Structural Study of the New Complex Oxides Ba$_{5-y}$Sr$_y$R$_{2-x}$Al$_2$Zr$_{1+x}$O$_{13+x/2}$ (R = Gd–Lu, Y, Sc)

R. V. Shpanchenko, A. M. Abakumov, and E. V. Antipov

Department of Chemistry, Moscow State University, 119899 Moscow, Russia

and

L. Nistor,[1] G. Van Tendeloo,[2] and S. Amelinckx

EMAT, University of Antwerp (RUCA), 2020 Antwerp, Belgium

New anion-deficient hexagonal perovskite-like complex oxides Ba$_5$R$_2$Al$_2$ZrO$_{13}$ (R = Gd–Lu, Y) and Ba$_{5-y}$Sr$_y$Sc$_{1.33}$Al$_2$Zr$_{1.66}$O$_{13.33}$ were synthesized and studied by X-ray powder diffraction, electron diffraction, and high-resolution electron microscopy. All the compounds have similar crystal structures based on the 10H close-packed (cchcc)$_2$ stacking of BaO$_{3-x}$ layers. The anion vacancies are located in the h-type lamellae and may occur either in an ordered or in a disordered manner, depending on the R^{3+} cation type. It is shown that the radius of the rare-earth element critically influences the composition and the possibility of ordering in the crystal structures of these compounds. High resolution electron microscopy revealed the presence of a large number of stacking defects, their number, and size, depending on the type of the rare-earth element. The crystal structures of these compounds can be formally described as intergrowth structures with an alternation of BaZrO$_3$ and β-Ba$_2$ScAlO$_5$-type blocks along the c axis. © 1995 Academic Press, Inc.

1. INTRODUCTION

In recent years a number of anion-deficient hexagonal perovskites ABO_{3-x} containing transition-metal B cations have been studied (1–3). In such structures the oxygen nonstoichiometry, i.e., the presence of oxygen vacancies, is realized due to the ability of the transition metal ions to exhibit different valences. The structure of the majority of the ABO_{3-x} oxides is based on the stacking of AO_3 layers with the periodic insertion of AO_{3-x} layers, which contain the oxygen vacancies.

A number of anion-deficient hexagonal perovskites

have been recently synthesized by the insertion of two different atom species with different valences in the B-cation sublattice. Examples of such complex oxides are β-Ba$_2$ScAlO$_5$ (4) and Ba$_2$InAlO$_5$ (5). In the structures of these compounds aluminium is tetrahedrally coordinated by oxygen. The tetrahedra result from the localization of oxygen vacancies in the AO$_{3-x}$ layers neighboring the layers of aluminum ions. The compound Ba$_7$Sc$_6$Al$_2$O$_{19}$ (6) has a structure of this type; it can be considered as the intergrowth of two different building blocks which alternate along the c axis, β-Ba$_2$ScAlO$_5$ and Ba$_3$Sc$_4$O$_9$. Various periodic stacking sequences of such blocks have been observed by high-resolution electron microscopy (7).

Very recently, the structure of the complex anion-deficient oxide Ba$_5$In$_2$Al$_2$ZrO$_{13}$ has been determined by means of X-ray diffraction (8), and it was shown to be an intergrowth structure of Ba$_2$InAlO$_5$ and BaZrO$_3$ lamellae which alternate along the c direction of the hexagonal structure.

In this paper we present the results of structural investigations of the anion-deficient perovskite-like compounds Ba$_{5-y}$Sr$_y$R$_{2-x}$Al$_2$Zr$_{1+x}$O$_{13+x/2}$ (R = Gd–Lu, Y, Sc) and we discuss some features of the formation of similar intergrowth structures. We have carried out the synthesis, the X-ray diffraction, and electron microscopy studies to clarify the influence of substitutions in the A and B frameworks on the matching of the intergrowth structural blocks and on the localization of anion vacancies. The use of β-Ba$_2$ScAlO$_5$-type and MZrO$_3$ (M = Ba, Sr) structural blocks is rather convenient for modeling the intergrowth structures, since epitaxy is possible along the contact plane between the two types of structural blocks. The first one has a particular structural fragment consisting of two corner-sharing tetrahedra with completely ordered oxygen vacancies. Ba(Sr)ZrO$_3$ has the ideal cubic perovskite structure, which is based on the (ccc) close-packing along the [111] direction of the cubic cell.

[1] On leave from the Institute of Atomic Physics, I.F.T.M., P.O. Box Mg-6 Magurele, 76900-Bucharest, Romania.

[2] To whom the correspondence should be addressed.

TABLE 1
Cell Parameters for $Ba_{5-y}Sr_yR_{2-x}Al_2Zr_{1+x}O_{13+1/2x}$ Compounds

Compound	a (Å)	c (Å)	V (Å^3)
$Ba_5Gd_2Al_2ZrO_{13}$	5.9807(1)	24.771(1)	767.2(3)
$Ba_5Dy_2Al_2ZrO_{13}$	5.9470(9)	24.817(7)	760.1(5)
$Ba_5Ho_2Al_2ZrO_{13}$	5.9547(7)	24.709(4)	758.8(3)
$Ba_5Er_2Al_2ZrO_{13}$	5.9462(6)	24.672(4)	755.5(3)
$Ba_5Tm_2Al_2ZrO_{13}$	5.9348(6)	24.635(3)	751.4(2)
$Ba_5Yb_2Al_2ZrO_{13}$	5.9269(6)	24.603(4)	748.5(3)
$Ba_5Lu_2Al_2ZrO_{13}$	5.9262(5)	24.611(4)	748.5(3)
$Ba_5Y_2Al_2ZrO_{13}$	5.9498(9)	24.70(2)	757.3(8)
$Ba_5Sc_{1.33}Al_2Zr_{1.67}O_{13.33}$	5.8495(9)	24.29(1)	719.9(5)
$Ba_{4.5}Sr_{0.5}Sc_{1.33}Al_2Zr_{1.67}O_{13.33}$	5.7981(1)	23.7547(3)	692.2(2)

2. EXPERIMENTAL

Polycrystalline samples were prepared by conventional solid state reaction. The starting materials $BaCO_3$, $SrCO_3$, R_2O_3 (R = rare earth), Al_2O_3, and ZrO_2 in appropriate molar ratios were mixed thoroughly, ground, and pelletized. The pellets were placed in Al_2O_3 crucibles and annealed in Naberterm furnaces in air at 1600°C for 20–80 h with intermediate regrinding. The samples were finally furnace cooled. X-ray powder diffraction investigations were carried out using a FR-552 camera ($CuK\alpha_1$ radiation; internal standard, germanium). Raw data for the structure determination were collected on a Stadi P. diffractometer with a rotating sample on a transmission goniometer, using a curved germanium monochromator and a scintillation counter. The RIETAN program (9) was applied for the crystal structure refinement by the Rietveld method with pseudo-Voigt profile functions. Samples for transmission electron microscopy investigations were prepared by crushing the pellets under alcohol and dispersing the fragments on copper grids covered with a holey carbon film. The double-tilting stage of the Philips CM-20 electron microscope has been used for electron diffraction. Nanoanalysis was performed on the same microscope equipped with an energy dispersive spectrometer LINK QX2000. High resolution images were obtained in the JEOL-4000 EX electron microscope operating at an accelerating voltage of 400 kV.

3. RESULTS

3.1. Synthesis and Chemical Analysis

A series of compounds with the general formula $Ba_{5-y}Sr_yR_{2-x}Al_2Zr_{1+x}O_{13+x/2}$ was obtained for R = Gd–Lu, Y, Sc; the compound with R = In was described previously (5). All these compounds have hexagonal cells with lattice parameters given in Table 1. Under the same conditions we failed to synthesize the compound with R = Tb. The majority of the investigated samples contained admixtures (<10%). For example, during the

investigation of the samples $5BaO + (0.5 + x)Y_2O_3 + Al_2O_3 + (2 - x)ZrO_2$ (x = 0; 0.5; 1.0; 1.5) polyphasic mixtures were detected, but no observal changes in the lattice parameters were found. This fact suggests the absence of a significant range of homogenity for the compound.

Chemical analysis by energy dispersive spectroscopy (EDS) on different grains of Gd- and Er-containing phases gave the approximate metal ratios $Ba:R:Al:Zr$: $21.6(9):8.0(5):9.2(8):4.5(3)$ and $19.8(9):7.5(2):8.1(7):4.1(3)$, respectively. One should note that some grains had a different composition containing an excess of zirconium. This fact will be further discussed.

We have carried out a refinement of the crystal structures for some of the oxides to determine the structural characteristics of these compounds.

3.2. General Structural Considerations

The crystal structures of the compounds under investigation are based on the 10H $(cchc)_2$ stacking of close-packed BaO_{3-x} layers and can be formally considered as intergrowth structures with alternating $BaZrO_3$-type and β-Ba_2ScAlO_5-type structural blocks along the c axis (Fig. 1). Such a consideration leads for instance to an ideal composition as $Ba_5R_2Al_2ZrO_{13}$ (i.e., $BaZrO_3$ + 2 ×
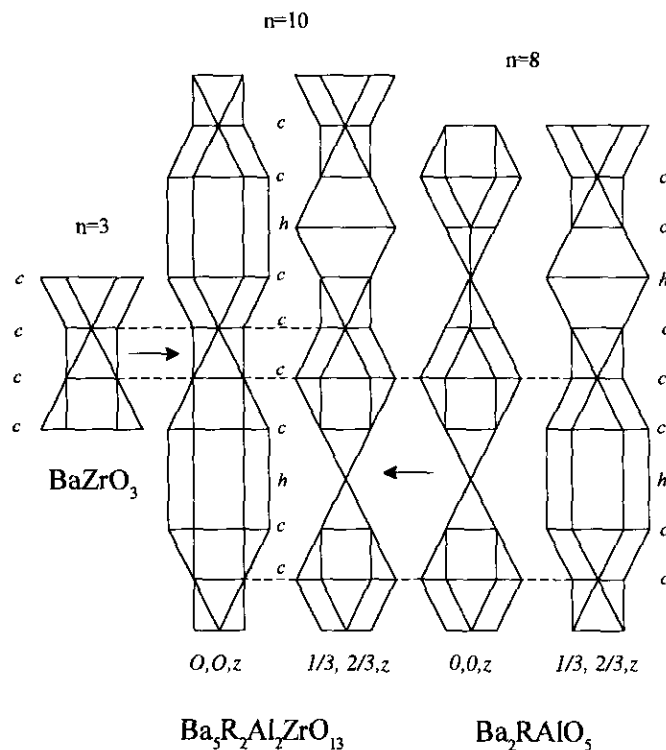

FIG. 1. The 10L $(cchcc)_2$ close packing of $Ba_5R_2Al_2ZrO_{13}$ (R=Gd–Lu, Y, Sc, In) as a result of intergrowth of 8L $(cchc)_2$ and 3L (ccc) close packings.
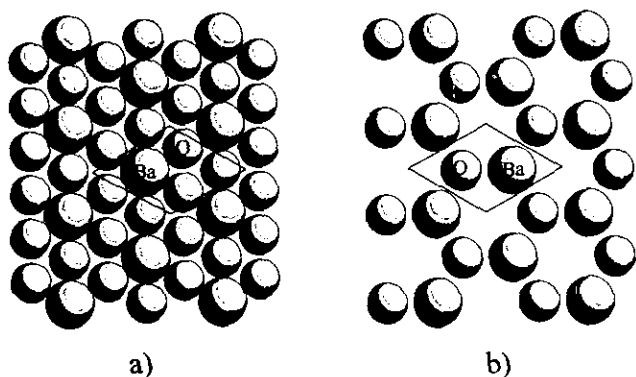
FIG. 2. Schematic representation of: (a) ideal BaO_3 and (b) aniondeficient $BaO\square_2$ layers.

β-Ba_2ScAlO_5). The localization of oxygen vacancies in x, y, $1/4(3/4)$ planes (h-type lamellae) leads to the a $BaO\square_2$ composition of these layers. A $BaO\square_2$ layer results from a BaO_3 layer if each triangle of oxygen is replaced by a single oxygen ion located in the center of this triangle. In the resulting $BaO\square_2$ layers each barium ion is surrounded by three oxygen ions, and vice versa, as shown in Fig. 2. This arrangement creates double layers of tetrahedra of oxygen having their common apices in the $BaO\square_2$ layer and their parallel triangular bases in the two adjacent BaO_3 layers. The aluminium ions, which prefer a tetrahedral coordination, occupy these pairs of tetrahedral interstices.

As a result of the ordering of oxygen vacancies a change of the Ba-atom arrangement occurs (Fig. 3). The polyhedron of Ba1 atoms (Fig. 3a) is half of a cuboctahedron, whereas the Ba3 atoms are situated in trigonal prisms (Fig. 3c) and have three equatorial oxygen neighbors with a bond length of about 3.4 Å. The rare earth and zirconium atoms are situated in the octahedral interstices formed by the oxygen atoms located in the BaO_3 layers. The schematic representation of the structure of $Ba_{5-y}Sr_yR_{2-x}Al_2Zr_{1+x}O_{13+x/2}$ (R = Gd–Lu, Y, Sc) compounds by means of coordination polyhedra is shown in
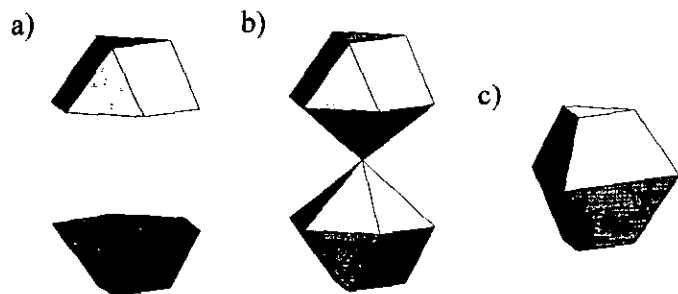
FIG. 3. Coordination arrangement of Ba atoms in $Ba_{5-y}Sr_yR_{2-x}Al_2$ $Zr_{1+x}O_{13+x/2}$ structures. Ba1 (a) and Ba3 (c) atoms in $Ba_5R_2Al_2ZrO_{13}$ (R=Gd–Lu, Y) structures; Ba1 atoms (b) in $Ba_{5-y}Sr_ySc_{1.33}Al_2$ $Zr_{1.66}O_{13.33}$ structures.

Fig. 4a, and by means of a ball model in Fig. 4b. The latter representation allows us to compare the high-resolution images with the structural model.

### 3.3. The Crystal Structure of $Ba_5Er_2Al_2ZrO_{13}$

The raw X-ray diffraction data contain peaks due to admixtures of Er_2O_3 and $BaAl_2O_4$ (maximal intensities less than 5%). Since the peaks due to these oxides overlap with the peaks of the main compound, the full profile refinement was carried out for the three phases simultaneously. The atomic positions for the Er_2O_3 and for the $BaAl_2O_4$ structures have been taken from (10) and (11), respectively. The crystallographic data and the main interatomic distances are listed in Tables 2, 3, and, 4 respectively. Experimental and difference profiles are shown in Fig. 5.

A completely ordered structure with an ideal composition $Ba_5Er_2Al_2ZrO_{13}$ is realized. Zr atoms are situated in the nondistorted octahedra at the origin; the Zr–O distance is 2.04 Å. Er atoms occupy the remaining slightly distorted octahedral interstices with $d_{Er-O} \sim 2.25$ Å. Such a separation is consistent with the difference between the ionic radii of Er^{3+} and Zr^{4+} (0.88 Å and 0.72 Å, respectively) in an octahedral arrangement.

The long Ba3–O3 distance (3.43 Å, arising from the tetrahedral coordination of Al atoms) leads to a large anisotropy of the thermal parameter for the Ba3 atoms in the a-b plane. This result follows from single-crystal data obtained for Ba_2InAlO_5 (5) and $Ba_5In_2Al_2ZrO_{13}$ (8). The refinement of the anisotropic thermal parameter for the Ba3 atoms resulted in a noticeable decrease of the R factors.

Identical ideal structures were found for the $Ba_5Lu_2Al_2$ ZrO_{13}, $Ba_5Gd_2Al_2ZrO_{13}$, and $Ba_5Y_2Al_2ZrO_{13}$ compounds.

3.4. The Crystal Structure of $Ba_{4.5}Sr_{0.5}Sc_{1.33}Al_2Zr_{1.67}O_{13.33}$
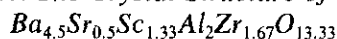
The sample with bulk composition $Ba_4SrSc_2Al_2ZrO_{13}$ contained $SrZrO_3$ (tetragonal) and $BaAl_2O_4$ together with the main phase. Polyphasic refinement was carried out to take into account the overlapping of the peaks for main and admixed phases. The atomic positions for the $SrZrO_3$ and $BaAl_2O_4$ structures were taken from (12) and (11), respectively. Crystallographic data and the main interatomic distances are listed in Tables 2, 3, and 5, respectively. Experimental and difference profiles are shown in Fig. 6.

In contrast to the $Ba_5Er_2Al_2ZrO_{13}$ structure the composition of this complex oxide was found (from structure refinement) to be $Ba_{4.5}Sr_{0.5}Sc_{1.33}Al_2Zr_{1.67}O_{13.33}$. This composition is similar to the one determined for the $Ba_5Sc_{1.33}Al_2Zr_{1.67}O_{13.33}$ oxide, if one takes into account a partial substitution of Ba atoms by Sr. The refinement of
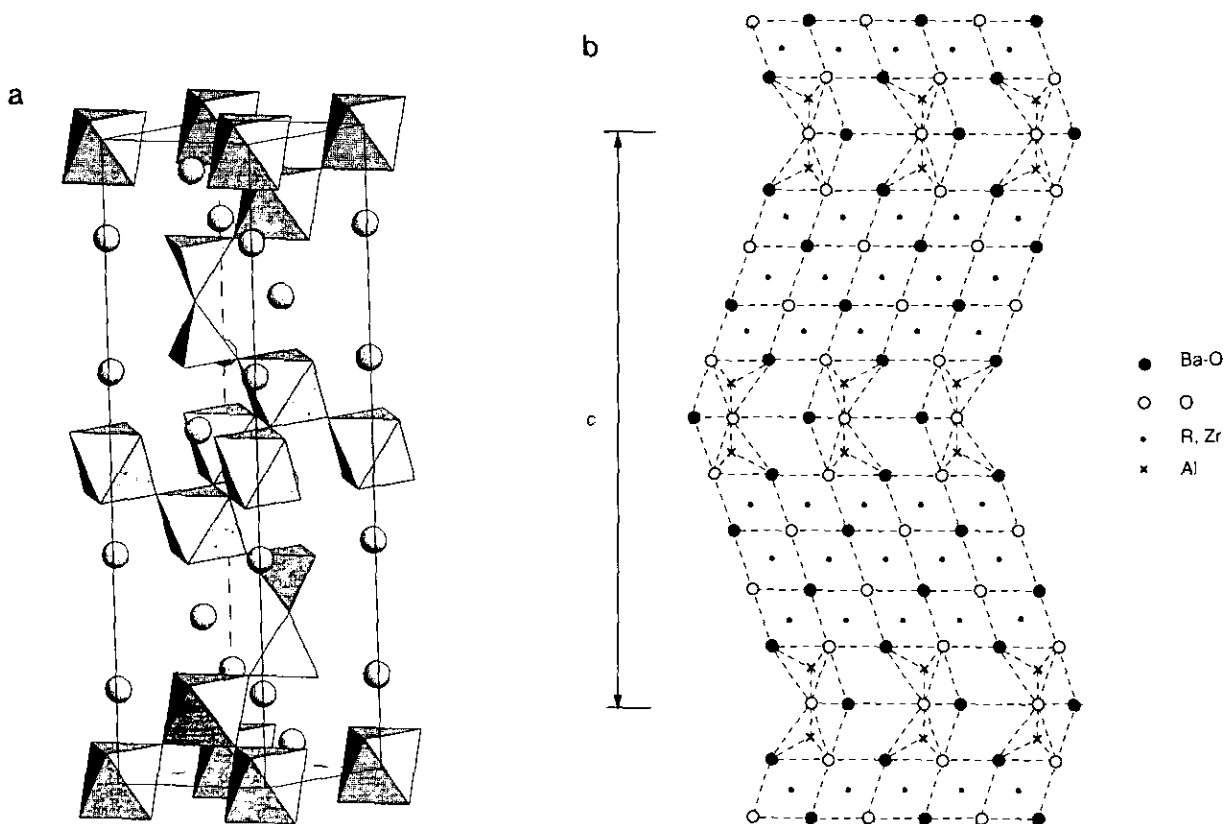
FIG. 4. Schematic representation of the structure of $Ba_{5-y}Sr_yR_{2-x}Al_2Zr_{1+x}O_{13+x/2}$ ($x = 0, 0.5$; R=Gd–Lu, Y, Sc) compounds: (a) by means of coordination polyhedra, where circles represent Ba atom positions, R and Zr atoms are located in the oxygen octahedra, and Al atoms in the oxygen tetrahedra; (b) in projection viewed along the close-packed rows.

the $2a$ and $4f$ positions with Zr and Sc atoms correspondingly led to values of the thermal parameters of 2.8 Å^2 and -1.9 Å^2. Therefore, a model of the structure with statistical occupancies of both positions has been chosen for the final refinement. Note that the resulting interatomic distances Sc–O and Zr–O are consistent with the obtained occupancies.

In comparison with the ideal composition $Ba_5R_2Al_2ZrO_{13}$, the main feature of this structure is the presence of extra oxygen atoms. These extra atoms are situated in the x, y, 1/4(3/4) planes. As a result, the composition of the $BaO\square_2$ layers is changed to $BaO_{1.33}\square_{1.67}$. O4 atoms are located in the $2b$ position with occupancy 1/3; they close the open polyhedra of Ba1 atoms to a 10-vertex polyhedron, as is shown in Fig. 3b. Also three additional equatorial oxygen atoms arise for the Ba3 atoms. However, the Ba3–O4 distance is also large (3.36 Å) and the Ba3 atoms have a strong anisotropic thermal parameter. The $4e$ positions are statistically occupied by Ba and Sr (3/4 + 1/4 respectively). All the other positions are occupied by Ba atoms only.

A similar structure was found for the compound $Ba_5Sc_{1.33}Al_2Zr_{1.67}O_{13.33}$ ($R_1 = 0.055$).

3.5. Electron Diffraction

In Fig. 7 we reproduce the electron diffraction patterns along the most relevant zone axes, [0001]*, [11$\bar{2}$0]*, and [10$\bar{1}$0]*, for a representative compound $Ba_5Sc_{1.33}Al_2Zr_{1.66}O_{13.33}$. Apart from small differences in the lattice parameters all compounds produce similar diffraction patterns. In the [0001]* zone axis pattern of Fig. 7a the first hexagon of spots is significantly weaker than the second one, which is consistent with the atomic arrangement in the BaO_3 layers. In the diffraction pattern of the [11$\bar{2}$0]* zone axis (Fig. 7b), the more intense spots in the basal and third rows, indicated by arrowheads, correspond to $l = 0, 10, 20 \ldots$; the corresponding interplanar distance is equal to the separation between successive BaO_3 layers. This indicates that the repeat distance along the c direction contains 10 BaO_3 layers. In the other dense rows $h\bar{h}0l$ with $h \neq 3$, the most intense spots are located in the vicinity of the diagonals of the rectangle formed by the indicated spots. This is a typical feature of subunit cell twinning of close-packed layers (13, 14). In the [10$\bar{1}$0]* zone diffraction patterns (Fig. 7c), the interspot spacing is twice that in the [11$\bar{2}$0]* zone pattern; this is consistent with the systematic absence of $l = 2n + 1$ spots. It also

TABLE 2
Crystallographic and Experimental Data for $Ba_5Er_2Al_2ZrO_{13}$ and $Ba_{4.5}Sr_{0.5}Sc_{1.33}Al_2Zr_{1.67}O_{13.33}$

	$Ba_5Er_2Al_2ZrO_{13}$	$Ba_4SrSc_{1.33}Al_2Zr_{1.66}O_{13.33}$
Space group	$P6_3/mmc$	$P6_3/mmc$
a (Å)	5.94761(5)	5.81770(7)
c (Å)	24.6604(2)	24.1947(3)
Z	2	2
V (Å^3)	755.5	709.2
Calculated density (g/cm^3)	6.04	5.43
Mode of refinement	Full profile	Full profile
Profile function	Pseudo-Voigt	Pseudo-Voigt
Min and Max 2θ (deg.)	$12 \le 2\theta \le 125$	$12 \le 2\theta \le 95$
Number of phases	3	3
Admixtures	$BaAl_2O_4$ (I)	$BaAl_2O_4$ (I)
	Er_2O_3 (II)	$SrZrO_3$ (tetr.) (II)
R factors		
R_I (main phase)	0.033	0.031
R_I (admixtures)	0.062 (I), 0.056 (II)	0.053 (I), 0.022 (II)
R_P, R_{wP}	0.052, 0.068	0.047, 0.064
Texture parameter along the [001] axis	1.35(2)	none

TABLE 3
Atomic and Thermal Parameters for $Ba_5Er_2Al_2ZrO_{13}$ (1) and $Ba_{4.5}Sr_{0.5}Sc_{1.33}Al_2Zr_{1.67}O_{13.33}$ (2)

Atom		Pos.	x/a	y/b	z/c	B_{iso}(Å^2)
Ba1	(1)	4e	0	0	0.3596(1)	1.8(1)
*	(2)		0	0	0.3579(4)	1.1(3)
Ba2	(1)	4f	2/3	1/3	0.5431(1)	1.5(1)
BaSr	(2)		2/3	1/3	0.5441(3)	1.0(2)
Ba3	(1)	2d	2/3	1/3	1/4	a)
	(2)		2/3	1/3	1/4	b)
Zr	(1)	2a	0	0	0	1.1(2)
ZrSc	(2)		0	0	0	0.4(5)
Er	(1)	4f	2/3	1/3	0.3967(1)	1.5(1)
ScZr	(2)		2/3	1/3	0.3993(7)	1.1(4)
Al	(1)	4f	2/3	1/3	0.8177(8)	1.5(4)
	(2)		2/3	1/3	0.817(2)	0.2(2)
O1	(1)	12k	0.508(1)	2x	0.6589(6)	3.4(3)
	(2)		0.510(3)	2x	0.653(1)	0.8(5)
O2	(1)	12k	0.314(4)	x/2	0.4498(7)	3.4
	(2)		0.328(8)	x/2	0.448(1)	0.8
O3	(1)	2c	1/3	2/3	1/4	3.4
	(2)		1/3	2/3	1/4	0.8
O4*	(2)	2b	0	0	1/4	0.8

BaSr = 3/4Ba + 1/4Sr   ScZr = 1/2Sc + 1/2 Zr
ZrSr = 2/3Zr + 1/3Sc   * = 0.333O

Anisotropic thermal parameters for Ba3 atoms

	β_{11}	β_{22}	β_{33}	β_{12}	β_{13}	β_{23}
a)	0.061(3)	0.061	0.005(1)	0.0305	0	0
b)	0.038(6)	0.038	0.002(3)	0.019	0	0

TABLE 4

Main Interatomic Distances (Å) for $Ba_5Er_2Al_2ZrO_{13}$

Bal	-O2	2.75(2)	×3	Zr	-O2	2.04(2)	×6
	-O1	3.009(8)	×6				
Ba2	-O2	2.93(2)	×3	Er	-O2	2.24(2)	×3
	-O2	2.98(2)	×6		-O1	2.26(1)	×3
	-O1	3.29(1)	×3				
Ba3	-O1	2.88(1)	×6	Al	-O3	1.67(2)	×1
	-O3	3.434	×3		-O1	1.73(1)	×3

shows that among the 000*l* spots, those with *l* = 2*n* + 1 are in fact produced by double diffraction, which is consistent with the observation that 000*l* spots in Fig. 7b are alternatingly weak and strong. The diffraction conditions are thus the following: $hh0l$ reflections are only present for *l* = 2*n*; also 000*l* reflections are allowed only for *l* = 2*n*, consistent with the space group $P6_3/mmc$, determined by X-ray diffraction.

The diffraction patterns for the structure showing defects are reproduced in Fig. 8. The zone axis is [11$\bar{2}$0]*, i.e., the same as in Fig. 7b. In the pattern of Fig. 8a, which refers to $Ba_5Lu_2Al_2ZrO_{13}$, the dense rows of spots are streaked, indicating a one-dimensional disorder of the layers. It suggests that the succession of BaO_3 and $BaO\square_2$ is perturbed, or stated otherwise, that the width of the twin lamellae is somewhat variable, as will be confirmed by real space imaging. Figure 8b, taken from a $Ba_5Gd_2Al_2$ ZrO_{13} crystallite, reveals the presence of supplementary reflections indicated by arrowheads. We will show below that this is due to the superposition of the normal diffraction pattern and that this is due to a cubic $Ba(Zr,R)O_{3-\delta}$, compound where *R* means rare earth. Fig. 8c, which refers to the $Ba_5Er_2Al_2ZrO_{13}$ compound, is a composite diffraction pattern and that this is due to a cubic $Ba(Zr,R)O_{3-\delta}$, compound where *R* means rare earth. Fig. 8c, which refers spots of intermediate brightness form twin related rectangular patterns. We shall show, using high resolution images, that the latter sets of spots are produced by areas containing $Ba(Zr,R)O_{3-\delta}$ in two twin related variants. The rows of weak, closely spaced spots refer to the 10H stacking.

3.6. High-Resolution Electron Microscopy

3.6.1. Perfect structures. High-resolution images were mainly obtained along the [10$\bar{1}$0] zone. Along this zone the structure is viewed in a direction parallel to the columns formed by the close-packed Ba–O–Ba–O rows (see Fig. 4b). Figure 9 gives as an example an image of the $Ba_5Lu_2Al_2ZrO_{13}$ compound. It directly reveals the alternating stacking of BaO_3 and $BaO\square_2$ layers. Ba–O–Ba–O columns are revealed as bright dots. Extra-bright dots mark the $BaO\square_2$ layers. They correspond to the twin interfaces of the polysynthetically twinned texture. In the thinnest part of the specimen the *B* cations in the octahedral interstices between the BaO_3 layers are also imaged as rows of weak dots.

This interpretation of the high-resolution images is supported by the computer simulation performed with the Mac Tempas software package. Figure 10 reproduces a matrix of computed images for the [10$\bar{1}$0] zone of the $Ba_{4.5}Sr_{0.5}Sc_{1.33}Al_2Zr_{1.67}O_{13.33}$ compound, realized for different thickness and defocus values. A Zr ion was chosen as the origin of the structural model. The simulated images are consistent with the model of the structure and confirm the interpretation of the high resolution images. It is particularly clear that the $BaO\square_2$ twin planes show up brighter at all thicknesses.

3.6.2. Stacking defects. Figure 11 reproduces high resolution images of the compounds $Ba_5Lu_2Al_2ZrO_{13}$ and $Ba_5Gd_2Al_2ZrO_{13}$; the corresponding diffraction patterns were reproduced in Fig. 8a and 8b.

The images show a variation in the spacing of the twin

TABLE 5

Main Interatomic Distances (Å) for $Ba_{4.5}Sr_{0.5}Sc_{1.33}Al_2Zr_{1.67}O_{13.33}$

Bal	-O4	2.609(9)	×1	ZrSc	-O2	2.08(4)	×6
	-O2	2.74(4)	×3				
	-O1	2.92(2)	×6	ScZr	-O2	2.07(5)	×3
Ba2	-O2	2.88(4)	×3		-O1	2.19(3)	×3
	-O2	2.92(5)	×6				
	-O1	3.07(3)	×3	Al	-O3	1.61(4)	×1
Ba3	-O1	2.94(3)	×6		-O1	1.74(3)	×3
	-O3	3.359	×3				
	-O4	3.359	×3				

Absolute intensity
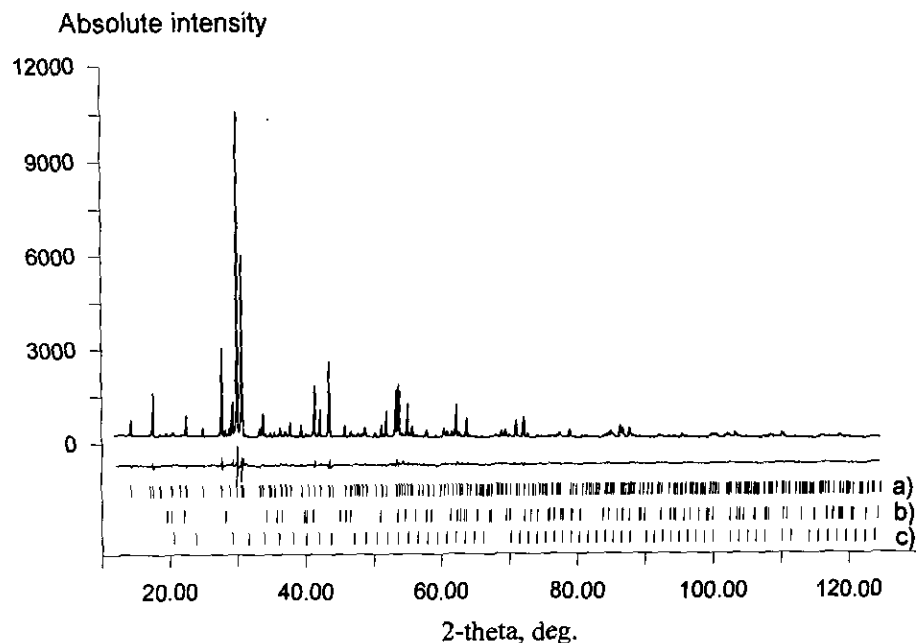

FIG. 5. Observed and difference X-ray profiles for $Ba_5Er_2Al_2ZrO_{13}$. Peak markers are given for: (a) $Ba_5Er_2Al_2ZrO_{13}$, (b) $BaAl_2O_4$, and (c) Er_2O_3.

interfaces. The most frequently occurring spacing corresponds to five BaO_3 layers, i.e., to the idealized structure. However, wider bands with 6, 7, or many more BaO_3 layers are not exceptional. It should be noted that no bands narrower than the normal ones were observed. The wider bands occur more frequently in the Gd and Er compounds than in the Lu compound. In the Sc-contain-

ing compounds almost no variation in intertwin spacing was noted.

The image contrast in these wider bands is identical to that observed within the twin bands of the long period structure. Optical diffraction patterns of the high resolution images taken from such zones allow one to identify the diffraction spots as belonging to a cubic stucture. The

Absolute intensity
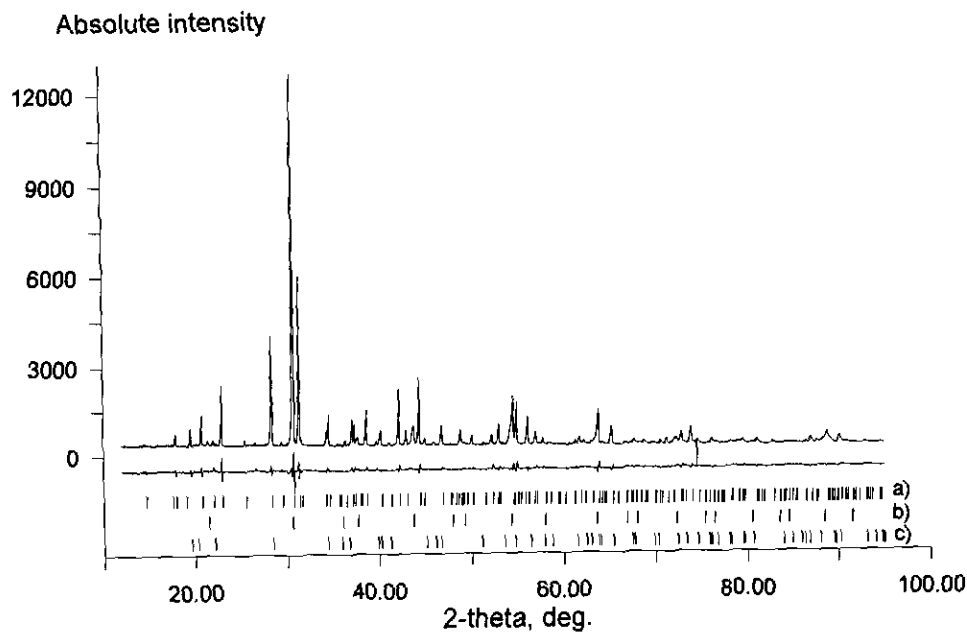
FIG. 6. Observed and difference X-ray profiles for $Ba_{4.5}Sr_{0.5}Sc_{1.33}Al_2Zr_{1.66}O_{13.33}$. Peak markers are given for: (a) $Ba_{4.5}Sr_{0.5}Sc_{1.33}Al_2Zr_{1.66}O_{13.33}$, (b) $BaAl_2O_4$, and (c) $SrZrO_3$.
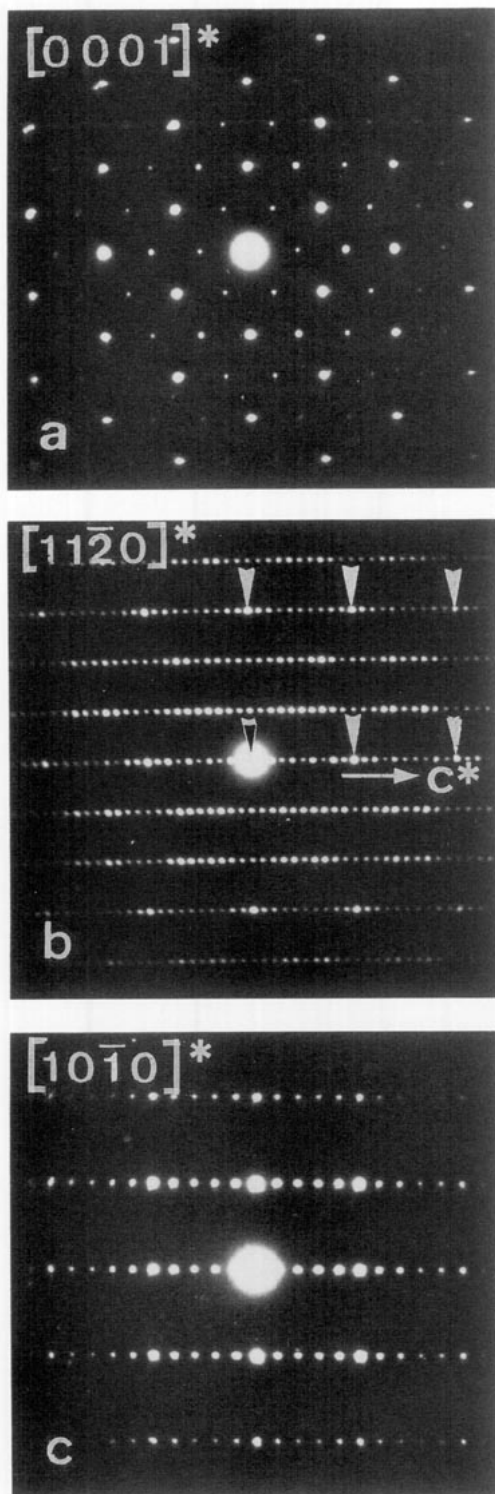
FIG. 7. Three sections of the reciprocal space of $Ba_5Sc_{1.33}Al_2$ $Zr_{1.67}O_{13.33}$ compound: (a) [0001]* zone, (b) [11$\bar{2}$0]* zone, (c) [10$\bar{1}$0]* zone.

interplanar spacing ratios and the angles between traces of planes correspond to the $[011]_c$ zone axis of a simple cubic lattice.

The composite diffraction pattern of Fig. 8c can now

be indexed as a superposition of three patterns. Two patterns, consisting of the most intense diffraction spots, originate from a simple cubic structure with lattice parameter $a \approx 4.2$ Å, and one weaker pattern is produced by the hexagonal long period structure. The two cubic diffraction patterns are twin related, the twin plane coinciding with the (0001) plane of the hexagonal long period structure. In the same way the extra spots in the diffraction pattern of Fig. 8b can be interpreted as due to the coexistence of the hexagonal and twinned cubic structures.

The structure present in the wider bands must thus be a simple cubic perovskite structure, essentially $Ba(Zr, R)O_{3-\delta}$, with a limited degree of isostructural substitution of Zr by rare earths. This cubic structure can be twinned on the $(111)_c$ planes which, like the $(0001)_h$ of the hexagonal structure, are close-packed layers with the same BaO_3 arrangement. The $(111)_c$ twin planes can adopt four different orientations, only one of which coincides with the $(0001)_h$ plane of the hexagonal structure.

In Fig. 12 the boxed area contains a striking rectangular 2D lattice of extra-bright dots. This area is surrounded by cubic $Ba(Zr, R)O_{3-\delta}$, imaged along a close-packed direction $[011]_c$, where the bright dots correspond to Ba–O columns. The small edge of the rectangular mesh, along the traces of the $(0001)_h$ planes, corresponds to the normal separation of bright dots, i.e., to the spacing of Ba–O columns viewed along a close-packed direction. The long edge of the rectangle covers three interlayer spacings. This array of prominently bright dots forms the image of a coincidence site lattice resulting from the overlap of two twin related areas of $Ba(Zr, R)O_{3-\delta}$ separated by an interface which is inclined with respect to the foil plane. Where the Ba–O column positions in the two parts coincide, these columns are continuous along the interface and imaged prominently. In noncoinciding sites, the Ba–O columns extend only in one part of the twin. The columns of B cations are not revealed under the imaging conditions of Fig. 12. Similar coincidence patterns of twin related overlapping zones have been already observed in silicon (15) and diamond (16) and in related face-centered cubic lattices (17). This is the first example for primitive cubic lattices. A corresponding diffraction pattern is formed by the superposition of the two patterns in twin relationship. Apart from the diffraction spots corresponding to the hexagonal structure, such a diffraction pattern is reproduced in Fig. 8c.

The ending bands of $Ba(Zr, R)O_{3-\delta}$ structure are coherently twinned with respect to the surrounding structure. They were found to contain a number of BaO_3 layers which is always a multiple of three; i.e., 6-, 9-, and 12-layered bands were observed. This restriction follows if one requires that the structure surrounding the terminating band should be continuous. This is illustrated in Fig. 13 for 6- and 9-layered bands. The relative shift along the

(0001) planes between successive BaO_3 layers is 1/3 of the repeat period and the shift is in the opposite sense for the twinned structure. Coincidence between twin and matrix at both coherent twin interfaces limiting the band can thus be achieved if the number of layers in the band is three fold.

The terminating band is in actual fact wedge-shaped, limited by an inclined interface, presumably another (111) twin plane of the cubic perovskite structure. As a result, in the overlap regions, the termination often exhibits the type of coincidence site lattice marked by bright dots in the high resolution image, as described above (Fig. 12). This is shown schematically in Fig. 14.

4. DISCUSSION

Perovskite-like intergrowth structures where different structural blocks alternate along the fourfold axis of the perovskite subcell are well known: for instance, the Aurivillius phases (perovskite and α-SnO-type blocks) and many high-temperature superconductors with perovskite, NaCl-type, or/and CaF_2-type blocks. This approach, of course, is rather formal, however, it takes into account a property of some ions to form stable coordination arrangements with appropriate geometrical characteristics.

In some structures of complex perovskite-like oxides with close-packed AO_3 layers it is possible to select fragments of sequences of close-packed layers. This fact allows one to consider such structures as intergrowth structures. Structural blocks of the β-Ba_2ScAlO_5-type and of the $BaZrO_3$-type can be formally selected in the crystal structures of $Ba_5R_2Al_2ZrO_{13}$ (Fig. 1). The stable tetrahedral coordination of Al atoms creates the possibility for the existence of a pair of corner-sharing tetrahedra Al_2O_7. The existence of these groups in the β-Ba_2ScAlO_5-type structural block requires a relation between the two constituent blocks as $(2 \times \beta\text{-}Ba_2ScAlO_5 + BaZrO_3)$.

In fact only two hexagonal perovskites containing Al_2O_7 groups were found, β-Ba_2ScAlO_5 and Ba_2InAlO_5. The complex oxides with similar compositions, Ba_2RAlO_5 (R = Nd–Nd, Y), have monoclinic structures (18, 19).

The ionic radii of rare earth elements critically determine the stability of the compounds under discussion. For example, the $Ba_5R_2Al_2ZrO_{13}$ phases with R=La–Eu
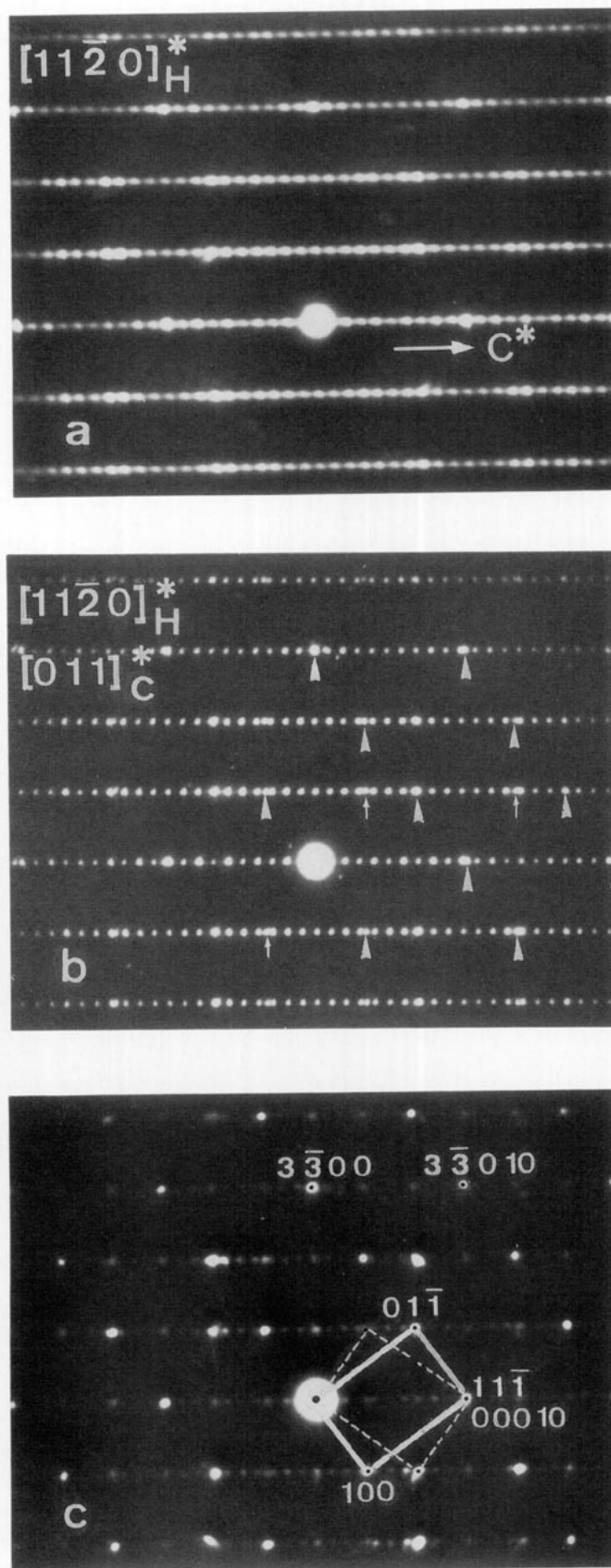
FIG. 8. Electron diffraction patterns of the $[11\bar{2}0]^*$ zone for (a) $Ba_5Lu_2Al_2ZrO_{13}$, (b) $Ba_5Gd_2Al_2ZrO_{13}$, (c) $Ba_5Er_2Al_2ZrO_{13}$ compounds, revealing the defect structure of these compounds. (a) shows streaks along the c^* axis; (b) and (c) represent the superposition of three diffraction patterns from the normal hexagonal and two twin related cubic structures. In (b) the matrix and twin spots are marked by arrowheads and small arrows, respectively. In (c) the hexagonal and cubic structures are indexed; the two twin related cubic structures are marked by rectangles, full lines for the matrix, dashed lines for the twin.
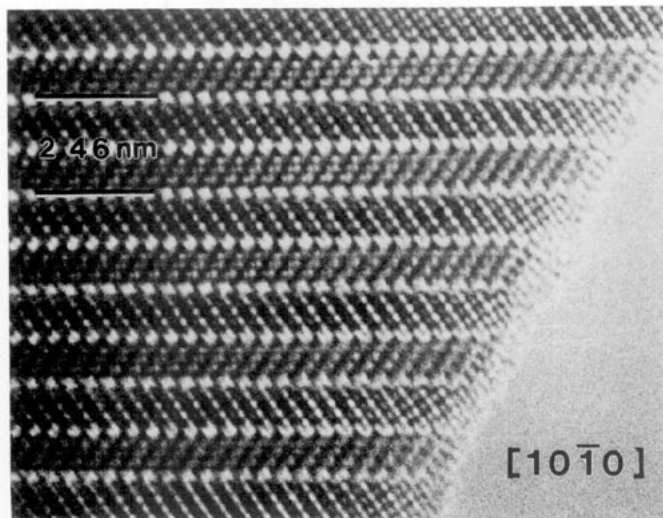
FIG. 9. High resolution image of the [10$\bar{1}$0] zone of the Ba$_5$Lu$_2$Al$_2$ZrO$_{13}$ compound. Bright dots show the alternative packing of BaO$_3$ and BaO$\square_2$ layers. Less bright dots represent the B cations columns.

have not been obtained. In this case, the ionic radii of the R^{3+} ions are too large to be placed in the octahedral interstices formed by the close-packed BaO$_{3-x}$ layers.

Moreover, for the compounds with R = Lu, Er, Gd, the high-resolution images revealed an increase in the number and the width of the stacking defects with increased radius of the rare earth ion. The widths of

the bands of cubic phase in the Ba$_5$Gd$_2$Al$_2$ZrO$_{13}$ compound can attain 30–50 nm. Such bands can be considered as resulting from the epitaxial intergrowth of cubic and hexagonal phases. Although Ba$_5$Er$_2$Al$_2$ZrO$_{13}$ and Ba$_5$Gd$_2$Al$_2$ZrO$_{13}$ contained a significant number of such wider cubic bands, BaZrO$_3$ was not detected in the X-ray diffraction spectra, presumably because these bands are too small to produce significant X-ray diffraction effects. On the contrary, electron diffraction patterns obtained from crystallites containing such bands revealed the presence of the two superimposed structures (cubic and hexagonal).

Since the real structure of some crystallites can differ from the ideal one, the compositions obtained from the EDS analysis on different crystallites could also be different. This has indeed been observed, some crystallites showing an excess of zirconium in the EDS spectra.

The epitaxy between the two structures can possibly be promoted by the partial substitution of Zr atoms by the rare earth ones in the cubic perovskite bands. This was confirmed by a slight increase in the lattice parameter of the admixed cubic perovskite (for instance ~4.204 Å in the Gd and Y patterns in comparison with the stoichiometric BaZrO$_3$ a = 4.193 Å).

From the point of view of vacancy ordering in the BaO$_{3-x}$ layers, significant differences in the ionic radii of the R^{3+} (R=Gd–Lu; 0.94–0.95 Å) and Zr^{4+} (0.72 Å) create the possibility for the formation of ordered structures in
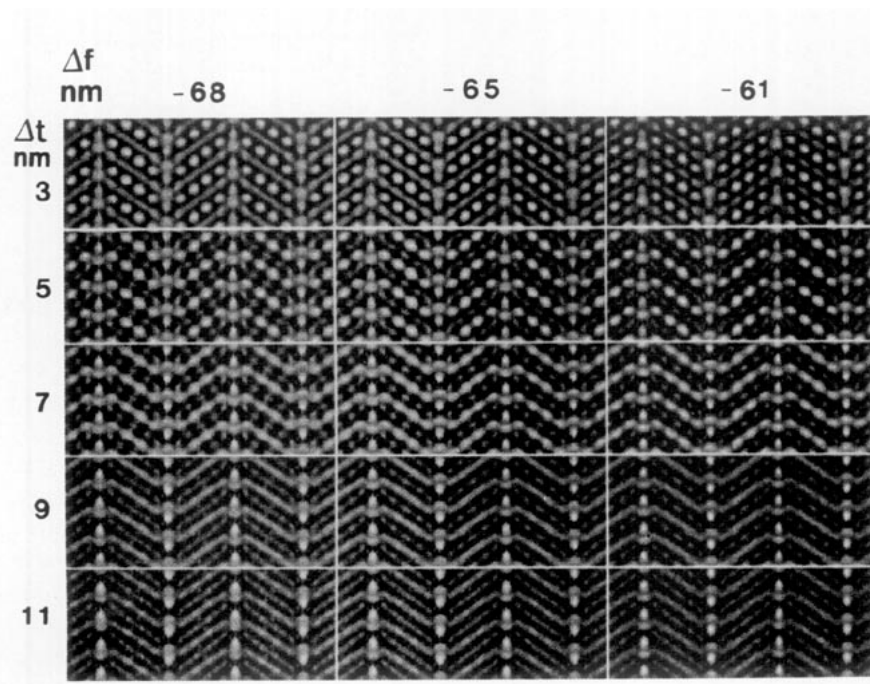

FIG. 10. Matrix of calculated high resolution images along the close-packed direction of the Ba$_5$Sc$_{1.33}$Al$_2$Zr$_{1.67}$O$_{13.33}$ compound for different defocus values (horizontal) and thicknesses (vertical); C_s = 1 mm, q = 0.55 mrad. The fit with the experimental images is obvious.

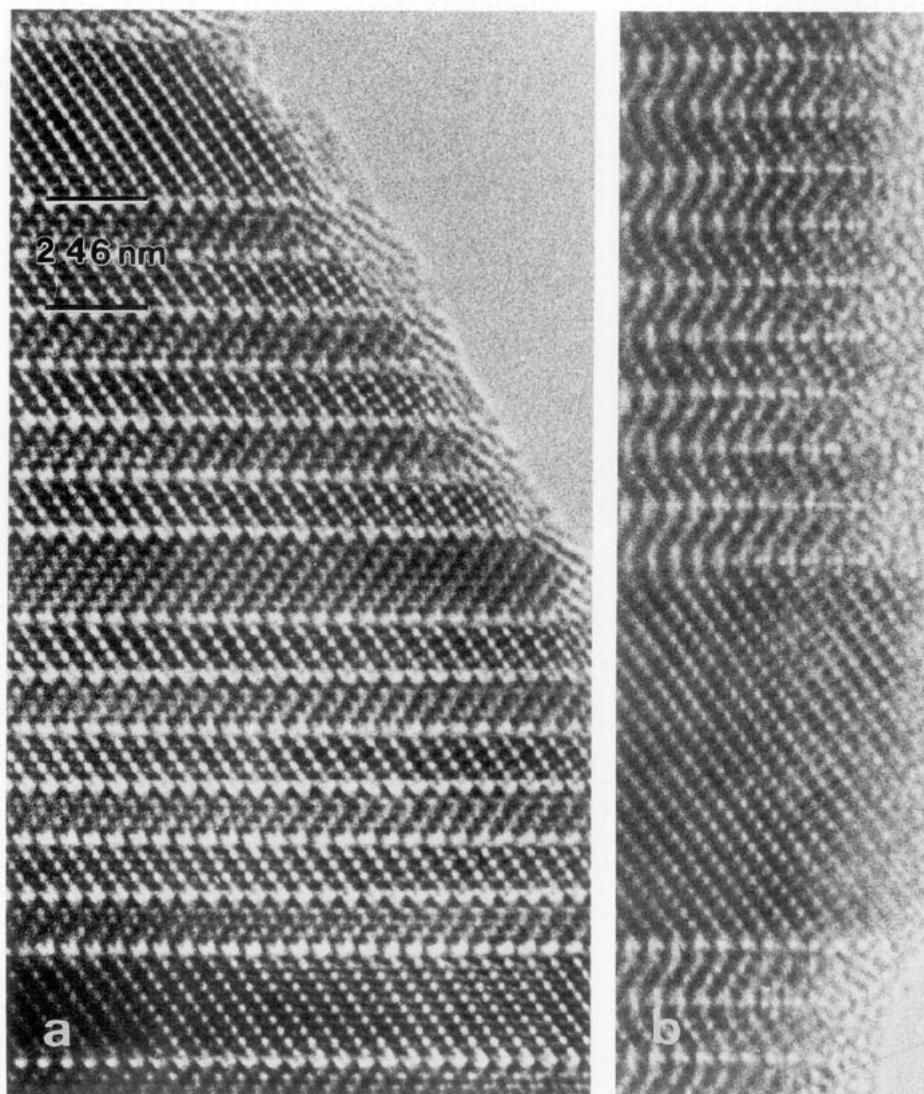FIG. 11. High resolution images along the [10$\bar{1}$0] zone for (a) $Ba_5Lu_2Al_2ZrO_{13}$ and (b) $Ba_5Gd_2Al_2ZrO_{13}$ compounds. The images show the alternation in stacking of the normal polysynthetically twinned structure with bands of a simpler apparently untwinned structure.

these layers. The rare earth atoms could be located in the octahedral interstices of the β-Ba_2ScAlO_5-type blocks, whereas Zr atoms could be placed in the $BaZrO_3$ blocks. This fact agrees also with the suggested model for the formation of intergrowth structures.

In contrast to the $Ba_5R_2Al_2ZrO_{13}$ (R=Gd–Lu, Y) struc- tures, the Sc-containing phases are more disordered. In these structures, Sc and Zr atoms jointly occupy octahe-dral sites, which can be understood if one considers the close values of their ionic radii, 0.73 Å and 0.72 Å, respec-tively. Possibly this is a reason why the compounds with R=Sc contain a minimum number of stacking defects.

The crystal structures of $Ba_{4.5}Sr_{0.5}Sc_{1.33}Al_2Zr_{1.67}O_{13.33}$ and $Ba_5Sc_{1.33}Al_2Zr_{1.67}O_{13.33}$ are practically identical. This suggests that a change of the A cation radius does not noticeably influence the matching of the intergrowth

blocks. The excess Sc which could arise in the normal $Ba_4SrSc_2Al_2ZrO_{13}$ bulk composition (used for the synthe-sis) compensates for the lack of zirconium in the $SrZrO_3$ structure. This is consistent with the change of the lat-tice parameters.

Charge balance requires oxygen deficiency in the $Ba_5R_2Al_2ZrO_{13}$ structures in comparison with the ideal perovskite composition ABX_3. In this case the oxygen vacancies are located in the h-type lamellae with the com-position $BaO\square_2$. The oxygen atoms in twofold positions form common vertices of two tetrahedra. The presence of a large number of oxygen vacancies results in the ab-sence of a rigid equatorial arrangement of barium atoms in the β-Ba_2ScAlO_5-type blocks and, as a consequence, in a large vibration amplitude of these atoms in a plane perpendicular to the c axis (i.e., a large anisotropy of the
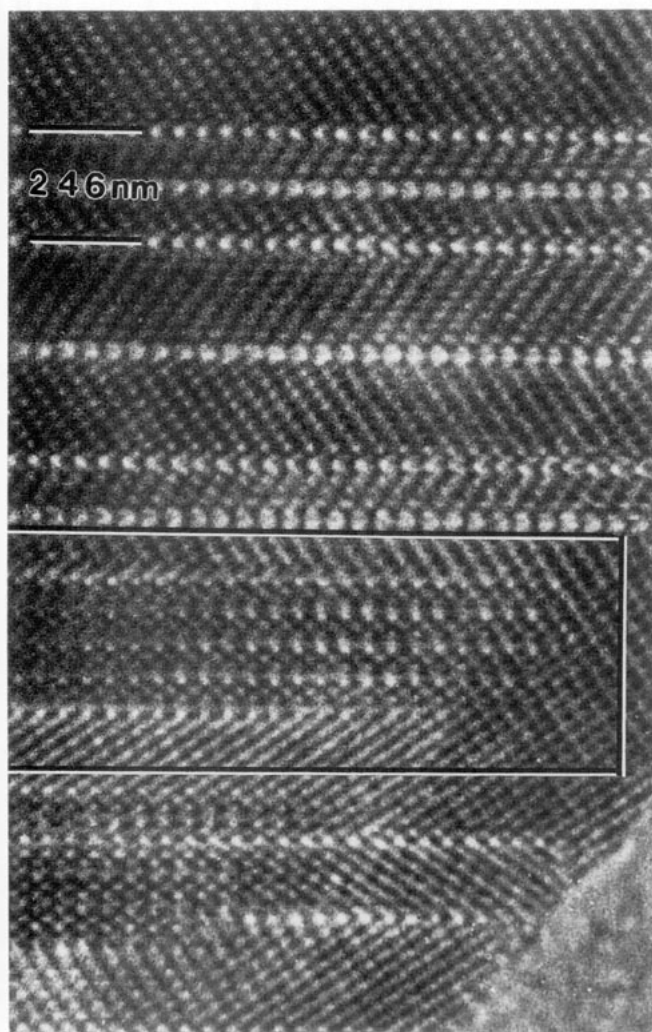
FIG. 12. High resolution images of the [10$\bar{1}$0] zone of the $Ba_5Er_2Al_2$ ZrO_{13} compound. The boxed area indicates changes in contrast due to overlapping of inclined twins giving rise to a coincidence pattern exhibiting threefold periodicity.

Therefore extra oxygen atoms occupy the 0, 0, 1/4 position and will close the nine-vertex polyhedron of the barium atoms.

A mixed occupation of B positions in the chc block is a feature of the $Ba_5In_2Al_2ZrO_{13}$ structure. The stability of the tetrahedral coordination for Al atoms and also the stability of the octahedral coordination for In atoms creates conditions for the delocalization of the oxygen atoms that form the common vertices of the two tetrahedra. As we have shown earlier (5), indeed this takes place. A shift
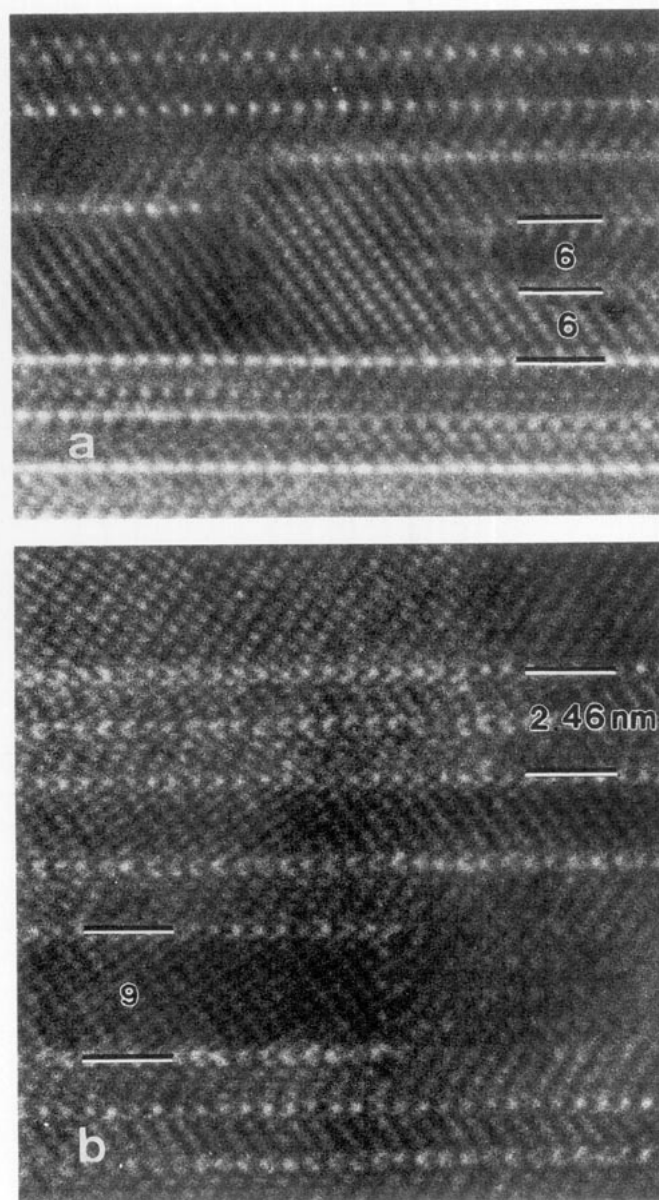

FIG. 13. High-resolution images of the [10$\bar{1}$0] zone for the $Ba_5Er_2Al_2$ ZrO_{13} compound showing the ending of $Ba(Zr, R)O_{3-\delta}$ bands in the normal subunit cell twinned structure. In these regions because the sample is thicker the atomic resolution is not well realized.
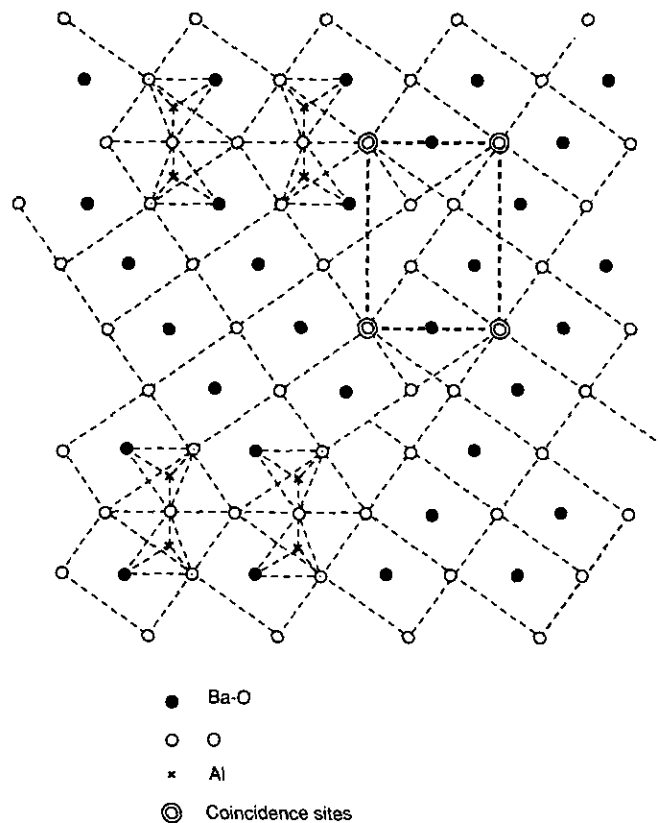
thermal parameters). A change of cation composition by the substitution of Sc^{3+} atoms by Zr^{4+} leads to the appearance of extra oxygen atoms. This heterovalent substitution results in a change of the number of oxygen vacancies and their localization.

When extra oxygen atoms are present, the composition of the anion-deficient layers becomes $BaO_{1.33}\square_{1.67}$. This process may occur by the delocalization of oxygen atoms in the 1/3, 2/3, 1/4 position (and their moving to the sixfold positions), or the occupation of the 0, 0, 1/4 (or the closest sixfold: x, $2x$, 1/4, $x \sim 0.1$) positions. However, the delocalization of oxygen atoms in the 1/3, 2/3, 1/4 position could not be realized owing to the existence of the stable tetrahedral arrangement of the Al atoms (if it is not a mixed position as it is realized in the $Ba_5In_2Al_2ZrO_{13}$ structure).

• Ba-O

○ O

× Al

◎ Coincidence sites

FIG. 14. Schematic representation of the structure of these compounds projected along the c axis; the configuration of Ba–O and oxygen columns is reproduced for both the hexagonal (left) and cubic (right) structures. The rectangular unit mesh of the $\Sigma 3$ coincidence pattern of the two twin related cubic structures is also indicated.

of Al/In atoms toward a statistically defined vertex (and a reduction of the metal–metal distance to 1.6 Å) can be explained by a statistical distribution of oxygen atoms. Possibly such an arrangement is unstable, since the $Ba_5In_2Al_2ZrO_{13}$ oxide was obtained only from partially melted samples.

To summarize, we distinguish three possibilities for the cation distribution in the B positions leading to three different ways of oxygen localization in the BaO_{3-x} layers in the structures of the type $Ba_{5-y}Sr_yR_{2-x}Al_2Zr_{1+x}O_{13+x/2}$.

Ideal Composition

(i) The B positions in the chc block are occupied only by Al atoms. The anion deficient layers have the composition $BaO\square_2$ and the oxygen atoms and vacancies are completely ordered, as in the crystal structure of $Ba_5R_2Al_2ZrO_{13}$, where $R = Gd–Lu$, Y.

(ii) The B positions in the chc block are occupied simultaneously by atoms with stable tetrahedral and octahedral

coordination. The anion-deficient layers have the composition $BaO\square_2$ but the oxygen atoms and vacancies are disordered, as in the crystal structure of $Ba_5In_2Al_2ZrO_{13}$.

Partial Substitution of R^{3+} by Zr^{4+} Atoms

(iii) The B positions in the chc block are occupied by Al atoms only. The anion-deficient layers have a composition $BaO_{1.33}\square_{1.67}$. The oxygen atoms and vacancies are partially ordered; the 1/3, 2/3, 1/4 position is fully occupied, the 0, 0, 1/4 position is partially occupied by extra oxygen atoms and vacancies; this is realized in the crystal structures of $Ba_{5-y}Sr_ySc_{1.33}Al_2Zr_{1.66}O_{13.33}$ ($y = 0$, 0.5)).

REFERENCES

1. T. Negas and R. S. Roth, *J. Solid State Chem.* **3**, 323 (1971).
2. A. J. Jacobson, *Acta Crystallogr. B* **32B**, 1087 (1979).
3. A. J. Jacobson and J. L. Hutchinson, *J. Solid State Chem.* **35**, 334 (1980).
4. R. V. Shpanchenko, E. V. Antipov, L. N. Lykova, and L. M. Kovba, *Vistnik Mosk. Univers. (Russ.) Ser. 2 Chim.* **31**, 555 (1991).
5. H. K. Müller-Buschbaum and M. Abed, *Z. Anorg. Allg. Chem.* **591**, 174 (1990).
6. R. V. Shpanchenko, E. V. Antipov, M. V. Paromova, and L. M. Kovba, *Russ. J. Inorg. Chem.* **36**, 797 (1991).
7. R. V. Shpanchenko, L. Nistor, G. Van Tendeloo, S. Amelinckx, E. V. Antipov, and L. M. Kovba, *J. Solid State Chem.* **113**, 193 (1994).
8. R. V. Shpanchenko, A. M. Abakumov, E. V. Antipov, and L. M. Kovba, *J. Alloys Compounds* **206**, 185 (1994).
9. F. Izumi, *Rigaku J.* **6**, 10 (1989).
10. A. Saiki, N. Ishizawa, N. Mizutani, and M. Kato, *J. Ceram. Assoc. Jpn.* **93**, 649 (1985).
11. A. J. Perrotta and I. V. Smith, *Bull. Soc. Fr. Mineral. Cristallogr.* **91**, 85 (1968).
12. M. Ahtee, A. M. Glazer, and A. W. Hewat, *Acta Crystallogr.* **34**, 752 (1978).
13. G. Van Tendeloo, D. Van Dyck, S. Kuipers and S. Amelinckx, *Phys. Status Solidi A* **101**, 339 (1987).
14. G. Van Tendeloo, D. Van Dyck, S. Kuipers, H. W. Zandbergen, and S. Amelinckx, *Phys. Status Solidi A* **102**, 597 (1987).
15. H. Bender, A. De Veirman, J. Van Landuyt, and S. Amelinckx, *Appl. Phys. A* **39**, 83 (1986).
16. W. Luyten, G. Van Tendeloo, S. Amelinckx, and J. L. Collins, *Philos. Mag. A* **66**, 899 (1992).
17. L. Nistor, G. Van Tendeloo, S. Amelinckx, and C. Cros, *Phys. Status Solidi A* **146**, 119 (1994).
18. L. M. Kovba, L. N. Lykova, E. V. Antipov, and M. G. Rozova, *Zh. Neorg. Khim. (Russ.)* **38**, 3137 (1984).
19. E. V. Antipov, L. N. Lykova, and L. M. Kovba, *Koord. Khim. (Russ.)* **11**, 1151 (1985).